

Enhancing the Conductivity and Thermoelectric Performance of Semicrystalline Conducting Polymers through Controlled Tie Chain Incorporation

Wenjin Zhu, Xinkai Qiu, Joonatan E. M. Laulainen, Hio-leng Un, Xinglong Ren, Mingfei Xiao, Guillaume Freychet, Petr Vacek, Dion Tjhe, Qiao He, William Wood, Zichen Wang, Youcheng Zhang, Zhengkang Qu, Jesika Asatryan, Jaime Martin, Martin Heeney, Christopher R. McNeill, Paul A. Midgley, Ian E. Jacobs,* and Henning Sirringhaus*

Conjugated polymers are promising materials for thermoelectric applications, however, at present few effective and well-understood strategies exist to further advance their thermoelectric performance. Here a new model system is reported for a better understanding of the key factors governing their thermoelectric properties: aligned, ribbon-phase poly[2,5-bis(3-dodecylthiophen-2-yl)thieno[3,2-b]thiophene] (PBTTT) doped by ion-exchange doping. Using a range of microstructural and spectroscopic methods, the effect of controlled incorporation of tie-chains between the crystalline domains is studied through blending of high and low molecular weight chains. The tie chains provide efficient transport pathways between crystalline domains and lead to significantly enhanced electrical conductivity of 4810 S cm^{-1} , which is not accompanied by a reduction in Seebeck coefficient or a large increase in thermal conductivity. Respectable power factors of $173 \mu\text{W m}^{-1} \text{ K}^{-2}$ are demonstrated in this model system. The approach is generally applicable to a wide range of semicrystalline conjugated polymers and could provide an effective pathway for further enhancing their thermoelectric properties and overcome traditional trade-offs in optimization of thermoelectric performance.

1. Introduction

Due to their relatively low thermal conductivities and their ease of tuning molecular structure—property relationships and controlling carrier concentrations, conjugated polymers are being investigated extensively as thermoelectric materials for operation near ambient temperature.^[1] However, their achievable thermoelectric performance remains inferior to state-of-the-art inorganic thermoelectrics, such as Bi_2Te_3 .^[2] Among the approaches for enhancing their electrical conductivities σ , Seebeck coefficients S and power factors $PF = S^2 \sigma$ the strategy of inducing uniaxial alignment of the polymer chains along the thermoelectric transport direction is particularly promising.^[3] Intrachain transport along the polymer backbone is much faster than interchain transport between polymer chains and as a result, the conductivity along the polymer chain alignment

W. Zhu, X. Qiu, H.-leng Un, X. Ren, M. Xiao, D. Tjhe, W. Wood, Z. Wang, Y. Zhang, Z. Qu, I. E. Jacobs, H. Sirringhaus
Optoelectronics Group
Cavendish Laboratory
University of Cambridge
JJ Thomson Avenue, Cambridge CB3 0HE, UK
E-mail: ij255@cam.ac.uk; hs220@cam.ac.uk
J. E. M. Laulainen, P. Vacek, P. A. Midgley
Department of Materials Science and Engineering
University of Cambridge
Cambridge CB3 0FS, UK

G. Freychet
University of Grenoble Alpes
CEA
Leti, Grenoble F-38000, France
Q. He, M. Heeney
Department of Chemistry
Imperial College London
London SW72AZ, UK
J. Asatryan, J. Martin
Centro de Investigaciones Tecnológicas (CIT)
Campus Industrial de Ferrol
Universidade da Coruña
Esteiro, Ferrol 15471, Spain
J. Martin
POLYMAT Paseo Manuel de Lardizabal 3
Donostia-San Sebastián 20018, Spain

 The ORCID identification number(s) for the author(s) of this article can be found under <https://doi.org/10.1002/adma.202310480>

© 2024 The Authors. Advanced Materials published by Wiley-VCH GmbH. This is an open access article under the terms of the [Creative Commons Attribution](#) License, which permits use, distribution and reproduction in any medium, provided the original work is properly cited.

DOI: 10.1002/adma.202310480

direction is generally significantly higher than that perpendicular to the alignment direction or that of polymer films with no chain orientation.^[3c,4] There have also been reports that the Seebeck coefficient can be enhanced along the chain alignment direction although the mechanism for this is currently not well understood.^[3a,b] However, for these beneficial enhancements to lead to an improved thermoelectric figure of merit $ZT = S^2 \sigma / T/\kappa$ strategies will need to be developed to limit the increase of the thermal conductivity along the chain alignment direction that typically accompanies the enhanced electrical conductivity.

The thermoelectric transport physics of semi-crystalline, aligned polymers is, however, complex: The topology of the charge transport pathways depends not just on how the aligned chains are packed and positioned with respect to each other within the crystalline domains, where interchain hopping is most likely to occur, but also on how charges can cross the more disordered amorphous regions/domain boundaries that separate the crystalline domains.^[5] Of particular importance to achieve high charge carrier mobilities is believed to be the presence of tie chains that connect adjacent crystalline domains and allow charges to cross between crystalline domains without having to undergo interchain hopping within disordered domains.^[6] However, in most aligned polymer systems that have been investigated in the literature, little is known about tie chains. Their presence is merely assumed, as tie chains are notoriously difficult to detect by direct structural methods, and their density cannot be controlled. What is required to better understand the thermoelectric physics of aligned polymers are model systems that allow control of tie chain density and a direct characterization of the impact of tie chains on both charge and thermal transport.

Here we present an experimental study of the thermoelectric transport physics of such a model system, the ribbon phase of poly[2,5-bis(3-dodecylthiophen-2-yl)thieno[3,2-b]thiophene] (PBTTT), which is one of the most highly ordered semicrystalline conjugated polymers with a microstructure that is reminiscent of that of semicrystalline polyethylene. PBTTT has a relatively small polymer dispersity index (PDI) and undergoes a phase transition into a smectic, liquid crystalline phase when annealed above 270 °C.^[6,7] The smectic chain arrangement is maintained during cooling into the crystalline phase and the crystalline domains take the shape of elongated ribbons in which individual chain-extended (or chain-folded) polymer chains are oriented perpendicular to the ribbon axis. Adjacent ribbons are separated by well-defined grain boundaries in which the chain ends are located (Figure 1a). Previous work using Scanning Kelvin Probe Microscopy (SKPM) has shown that these grain boundaries between ribbons constitute bottlenecks for charge transport.^[8] The polymer chains (and ribbons) can be uniaxially aligned by depositing the polymer by blade-coating.^[7] Here we demonstrate that this very well-defined model system, which has been widely studied for applications in field-effect transistors,^[6,7] but not yet for thermoelectrics, allows the controlled incorporation of tie chains between adjacent crystalline domains by using a blend of

two molecular weights (M_n) of PBTTT, a relatively low molecular weight close to the maximum molecular weight up to which the ribbon crystals remain chain extended, and chains of higher molecular weight, that are incorporated to act as tie chains (Figure 1a).

To study the thermoelectric transport physics, we used ion-exchange doping to control the charge carrier concentration. In this doping method the aligned, ribbon-phase polymer film is exposed to a doping solution that contains an oxidative molecular dopant and an ionic liquid. The molecular dopant induces electron transfer from the polymer, but the molecular radical anion is then exchanged with the anion of the ionic liquid, which acts as the charge stabilizing counterion for the mobile hole polarons on the polymer chains. The ion-exchange doping method achieves nearly 100% ion exchange efficiency and has a number of advantages over conventional molecular doping;^[9] its most relevant characteristic in the context of this work is that it maintains the highly crystalline microstructure of PBTTT over a wide range of carrier concentrations, even at the highest doping concentrations when about one charge per repeat unit is incorporated. Huang et al. previously achieved high thermoelectric power factors of $137.1 \mu\text{W m}^{-1} \text{K}^{-2}$ on terraced phase, ion-exchanged doped PBTTT that was aligned by mechanical rubbing.^[3a]

Here we studied the thermoelectric properties of aligned, ion-exchange-doped ribbon phase PBTTT with blends of different molecular weight components. We demonstrate that in blended films higher electrical conductivities (up to 4810 S cm^{-1}), Seebeck coefficients and thermoelectric power factors of up to $173 \mu\text{W m}^{-1} \text{K}^{-2}$ can be achieved than in films with single component molecular weights. We investigate the underpinning thermoelectric transport physics, including structural and spectroscopic characterization, to better understand how controlled tie chain incorporation can be used to enhance the thermoelectric performance of aligned conjugated polymers.

2. Results

2.1. The Clean Model of Tie Chains Incorporated PBTTT

The ribbon-phase PBTTT films were aligned by blade coating. We optimized the blade coating conditions (shear speed and substrate temperature) to maximize the degree of chain alignment; we obtained highly aligned films with a dichroic ratio of the neutral $\pi-\pi^*$ absorption peak in polarized optical spectroscopy > 10 (Figure S1, Supporting Information) and verified the uniformity of alignment of the films by polarized optical microscopy (Figure S2, Supporting Information). The films were doped by ion-exchange using $\text{FeCl}_3/\text{BMP}:\text{TFSI}$ in acetonitrile (Figure 1b, for experimental details, see experimental section). To control the concentration of tie chains we used blends of two different molecular weights, including a first component P1 with M_n of 28 kDa (PDI = 1.45) and a second P2 component with M_n of 35 kDa (PDI = 1.68) as measured by gel permeation chromatography (GPC). We selected P2 to have a significantly ($>25\%$) higher molecular weight than P1 to encourage the incorporation of P2 chains as tie chains into the crystalline ribbons formed by P1. We adjusted the ratios between P1 and P2 in the blend films and compared them to reference films comprising just P1 and P2. Fast scanning chip calorimetry (FSC), a form of differential scanning

C. R. McNeill
Department of Materials Science and Engineering
Monash University
Clayton, Victoria 3800, Australia

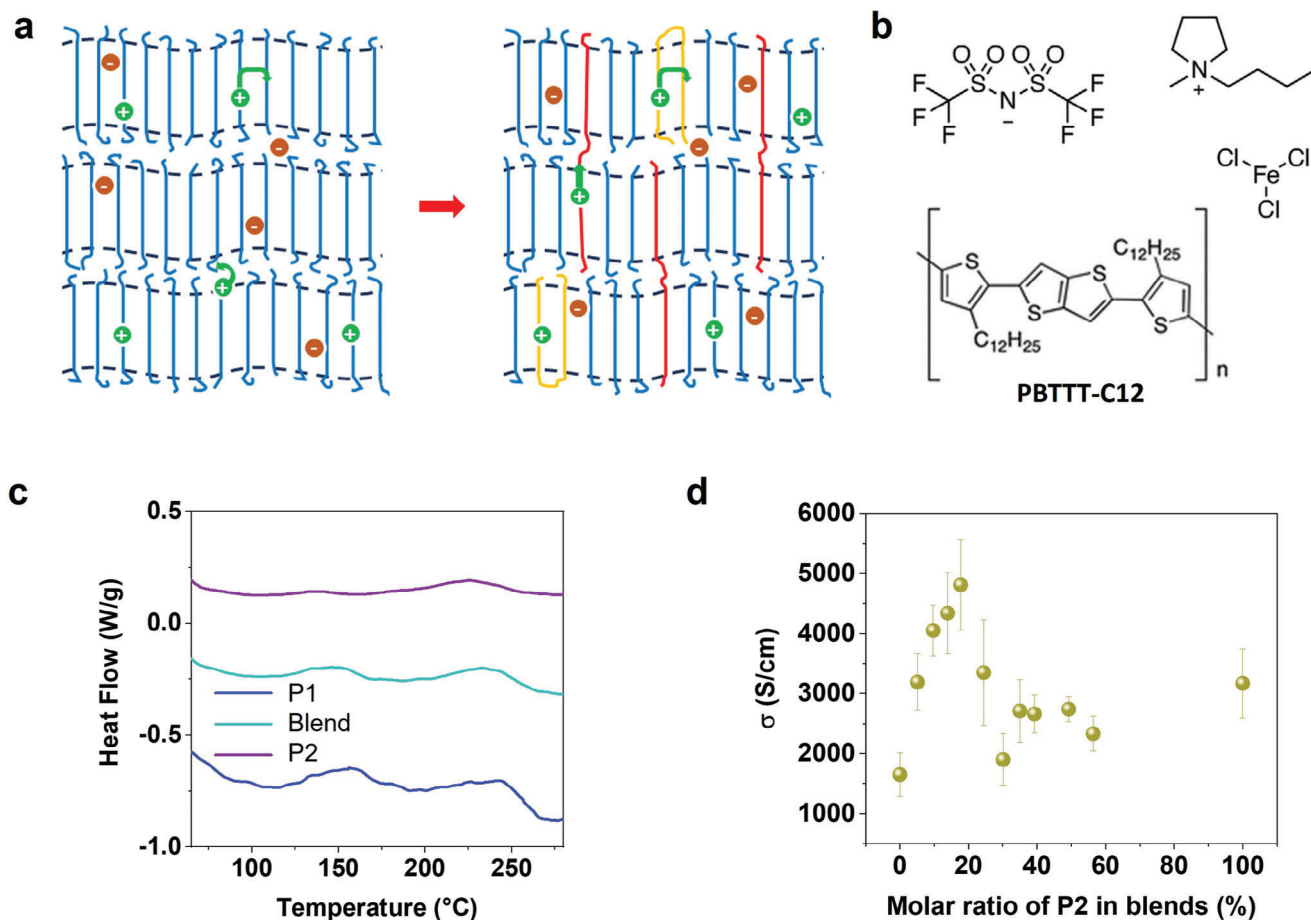


Figure 1. Aligned ribbon-phase PBTTT model system for studying the effect of controlled incorporation of tie chains on conductivity: a) Schematic of the aligned ribbon-phase with a single, low molecular weight component (left) and with a blend of two components of different molecular weight. Tie chains are illustrated in red and hairpin chain folds in orange. b) Chemical structures of PBTTT-C₁₂ and the molecules used in ion-exchange doping, FeCl₃, BMP, and TFSI. c) Differential scanning calorimetry (DSC) measurements on the undoped polymers, cooling rate of 10° min⁻¹. d) Dependence of the electrical conductivity of the blend films on the molar ratio of P2.

calorimetry (DSC) that is applicable to thin films,^[10] was used to investigate the thermal transitions (Figure 1c). P1 and P2 films both exhibit two exotherms on cooling, but at distinctly different temperatures of 156 and 244 °C (P1) and 139 and 227 °C (P2). The two corresponding transitions in blend films occur at temperatures of 149 and 234 °C. The different DSC transition temperatures were validated by temperature-dependent atomic force microscopy (AFM) measurements (Figure S3, Supporting Information). Our observation, that the DSC of the blend is not a combination of the DSCs of P1 and P2, but exhibits distinct transition temperatures, suggests clearly that in the blend films, there is no phase separation into P1 and P2 domains, but that the two molecular weight components are intimately mixed in the blend films. This is an important requirement for this system to be a controlled model system for tie chain incorporation. P1 exhibits the highest thermal transition temperatures and the most pronounced DSC peaks, this suggests that P1 has the highest degree of crystallinity, followed by the blends and finally by P2; this is likely to manifest a slower crystallization kinetics and higher viscosity in the melt induced by the presence of higher M_w chains.

The key observation that motivated this study is the evolution of the conductivity of the blend films as a function of the molar ratio (calculated using the number of polymer chain repeat units) of P2 (Figure 1d). Neat P1 and P2 films already reach relatively high electrical conductivities of 1650 and 3170 S cm⁻¹, respectively. However, surprisingly, as the ratio of P2 in the blend films increases, the electrical conductivity increases to a peak value of 4810 S cm⁻¹ at a composition of 17.1 mol% of P2, more than 2.5 times the conductivity of neat P1. As the P2 content further increases the conductivity decreases and reaches a near constant value above P2 concentrations of ≈ 35 mol%. In the following figures (as well as in Figure 1c) all the data for blend films are for the optimum composition that leads to the maximum conductivity.

Our hypothesis to explain the striking increase in conductivity in the blend films over both P1 and P2 neat films is that in all films the transport is limited by the grain boundaries between the ribbons^[8] and in P1 films the grain boundaries are particularly resistive due to the small PDI leading to a very low density of tie chains (Figure 1a (left)). The blending of the higher MW component into the lower MW polymer increases the

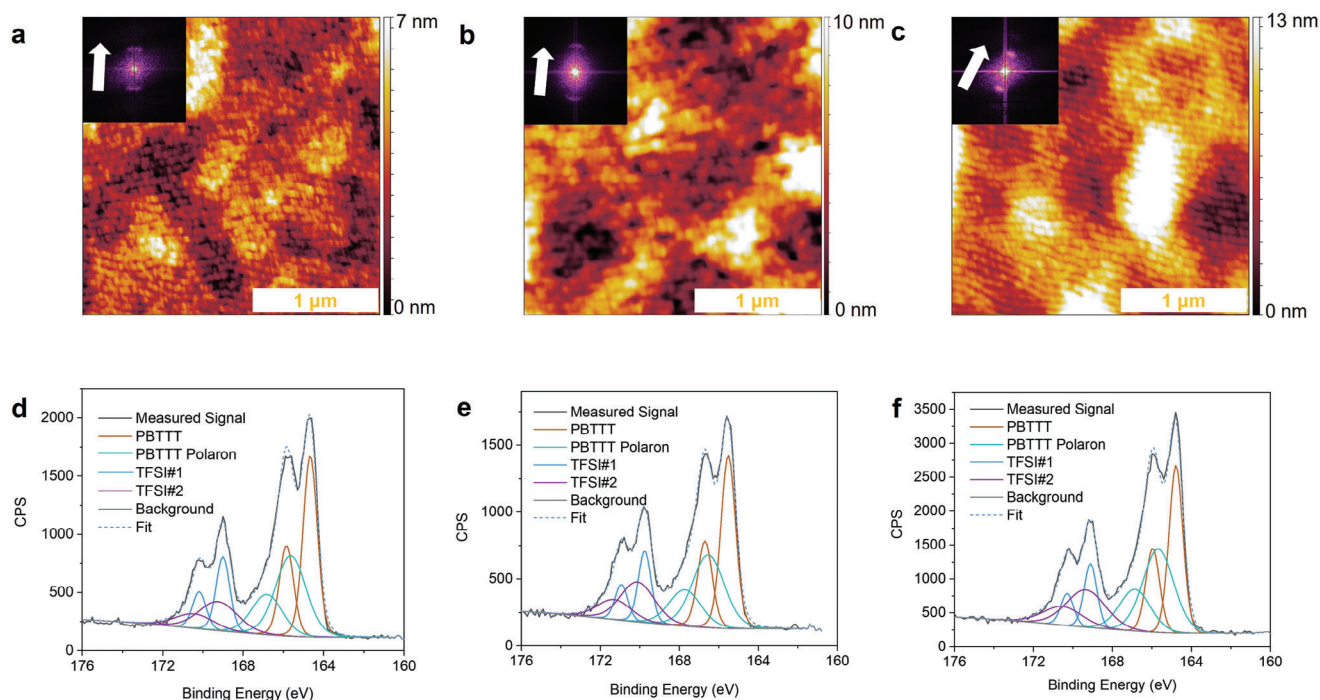


Figure 2. Comparison of surface morphology and carrier concentration for films of different molecular weight distribution: a–c) AFM images and the corresponding Fast Fourier Transform (FFT) images (insets) of aligned and undoped P1, blend, and P2 films, respectively. The white arrow indicates the chain alignment orientation. d–f) Corresponding sulfur 2p XPS spectra of aligned and undoped P1, blend, and P2 films, respectively. The measured spectra are fitted to components with different chemical shifts as explained in the text.

concentration of tie chains that are long enough to bridge the crystalline ribbons and facilitate the transport of charges between them (Figure 1a (right)). This seems a plausible hypothesis but, unfortunately, it is extremely difficult to observe tie chains directly in any microstructural measurement. To prove our hypothesis we therefore undertook a series of careful structural and spectroscopic measurements to probe any differences in the microstructure of the three different polymer films that could potentially provide alternative explanations for the observed behavior.

2.2. The Morphological and Microstructural Characterization

AFM revealed clear and uniform ribbon formation in all three films (Figure 2a–c). The ribbons appear as regions of elevated height separated by grain boundary regions of reduced height, which are aligned preferentially perpendicular to the blade coating direction indicated by the white arrow. The corresponding ribbon periodicity manifests itself as two well-defined, off-centered peaks in the Fourier transform of the AFM images (insets). The white arrows indicate the blade coating direction, that is, the direction of chain alignment. Statistical analysis of the ribbon widths averaged over three different samples and scan areas of each polymer (Figure 2a–c, Figure S4, Supporting Information) revealed similar periodicity of 68.9 ± 0.4 nm (P1), 71.8 ± 0.1 nm (blends), and 68.9 ± 0.4 nm (P2) despite the fact that P2 has significantly higher molecular weight than P1. This suggests that the polymer chains in P1 films are close to chain extended; the expected length of a straight chain of PBTTT with a molecular

weight of $M_n = 28$ k is 58 nm, which is consistent with the measured AFM periodicity if one takes into account the finite width of the grain boundary that accommodates the longer chains in the distribution. In P2 films, on the other hand, the majority of chains must contain hairpin chain folds (indicated in orange in Figure 1a, which are reported to be more significant for chains with higher molecular weights^[11]), because they exhibit a very similar ribbon width than P1 films. The small, but statistically significant increase in the ribbon width in blend films, compared to both P1 and P2, could indicate that in the blends the longer P2 chains are not primarily incorporated through hairpin chain folds, but as tie chains, which have a straightening effect on the adjacent P1 chain ends in the grain boundaries.

To quantify the doping concentrations X-ray photoemission spectroscopy (XPS) has previously been identified as one of the most accurate methods.^[12] Both TFSI and PBTTT contain sulfur atoms with a clearly resolved chemical shift, which allows quantifying the molar ratio of TFSI to PBTTT from peak fitting of the S 2p signal (Figure 2d–f). Before XPS measurements, we washed the surface of the films in acetonitrile to eliminate any residues on the surface. For the peak fitting, we used separate 2p doublet components for each of the neutral PBTTT chain segments and PBTTT radical cations and separate components for the two sulfur atoms on TFSI.^[12] The calculated molar doping ratio is around one ion per monomer for all 3 samples, with only minor differences of $8.5 \times 10^{20} \text{ cm}^{-3}$ (blend), $8.3 \times 10^{20} \text{ cm}^{-3}$ (P2) and $7.6 \times 10^{20} \text{ cm}^{-3}$ (P1), that may not be statistically significant. These results demonstrate that our chosen system is indeed a suitable model system to investigate the effect of tie chain

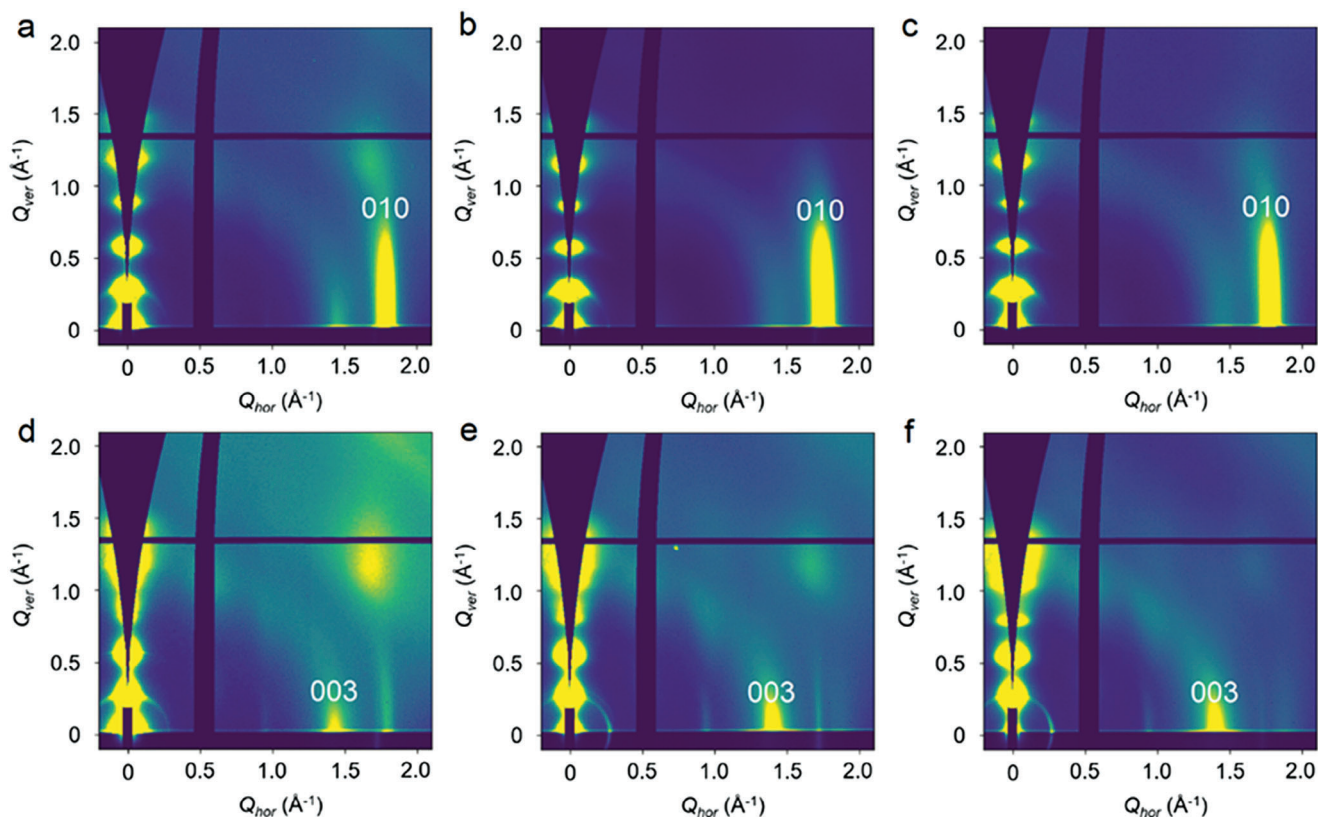


Figure 3. Comparison of crystalline order and paracrystallinity of films by GIWAXS: Measurements with X-rays incident along the chain alignment direction a) P1, b) blend, c) P2 and perpendicular to the chain alignment direction d) P1, e) Blend, f) P2.

incorporation on the thermoelectric properties, because of the absence of major changes in morphology and/or carrier concentration upon blending that would otherwise dominate the transport properties.

Grazing incidence wide-angle X-ray scattering (GIWAXS) was used to compare the crystalline order of the three films. For X-rays incident along the blade-coating direction a strong (010), π - π stacking diffraction and only a weak (003) backbone diffraction peak were observed in-plane in all three films (Figure 3a-c), while for X-rays incident perpendicular to the blade coating direction the (003) backbone is much stronger and the π - π stacking peak is weak (Figure 3d-f). This indicates that the blended films exhibit a similarly high in-plane chain alignment than the neat films.^[13] We extracted the paracrystallinities $g_{\pi-\pi}$ for the π - π stacking (Table S1, Supporting Information). $g_{\pi-\pi}$ quantifies the standard deviation of the π - π stacking distances across the crystalline domains (normalized by the average stacking distance). It determines the degree of off-diagonal, energetic disorder that is encountered by charges transferring between chains in the crystalline domains^[14] and has been found to be closely correlated with electrical conductivity.^[12] All three films exhibit very small $g_{\pi-\pi}$ values between 6.3% and 7.1% in their doped state (Table S1, Supporting Information) with only small differences between the three samples reflecting the high degree of structural order in the doped ribbon phase films. The $g_{\pi-\pi}$ value is slightly smaller in P1 films than in the blends, this is consistent with the higher degree of crystallinity observed

in the DSC. However, this small difference can clearly not explain the strong conductivity increase upon blending observed in Figure 2.

We employed 4D scanning transmission electron microscopy (4D-STEM) imaging to acquire diffraction patterns of individual ribbons and of the grain boundaries between them. Thin films were deposited by blade coating onto polystyrene sulphonate (PSS) coated substrates, lifted off in water, transferred onto TEM grids, and were then annealed into the ribbon phase while on the TEM grids. In the local diffraction patterns (inset of Figure 4a,d) we observe evidence for clear chain alignment with strongly anisotropic π - π stacking and backbone diffractions. In the annular dark field (ADF) images of both P1 (Figure 4a,b) and blend films (Figure 4d,e) the ribbon structure is clearly visible, and the ribbon periodicity is extracted to have similar values of around 70 nm than in the AFM images. Interestingly, in the local diffraction patterns, we observed strong interchain ordering and π - π stacking diffractions at all points crossing from one ribbon to the next, with only a relatively small reduction in intensity in the center of the grain boundary. The grain boundaries in the blend films appear particularly narrow in the ADF images and were estimated to have a width less than 5 nm. This suggests that even in the grain boundaries pronounced chain alignment is present. Exact values for the grain boundary width are uncertain due to the finite probe size necessary to have sufficient diffraction resolution. The grain boundary regions in P1 were found to be slightly, but significantly wider (by ≈ 2.0 nm)

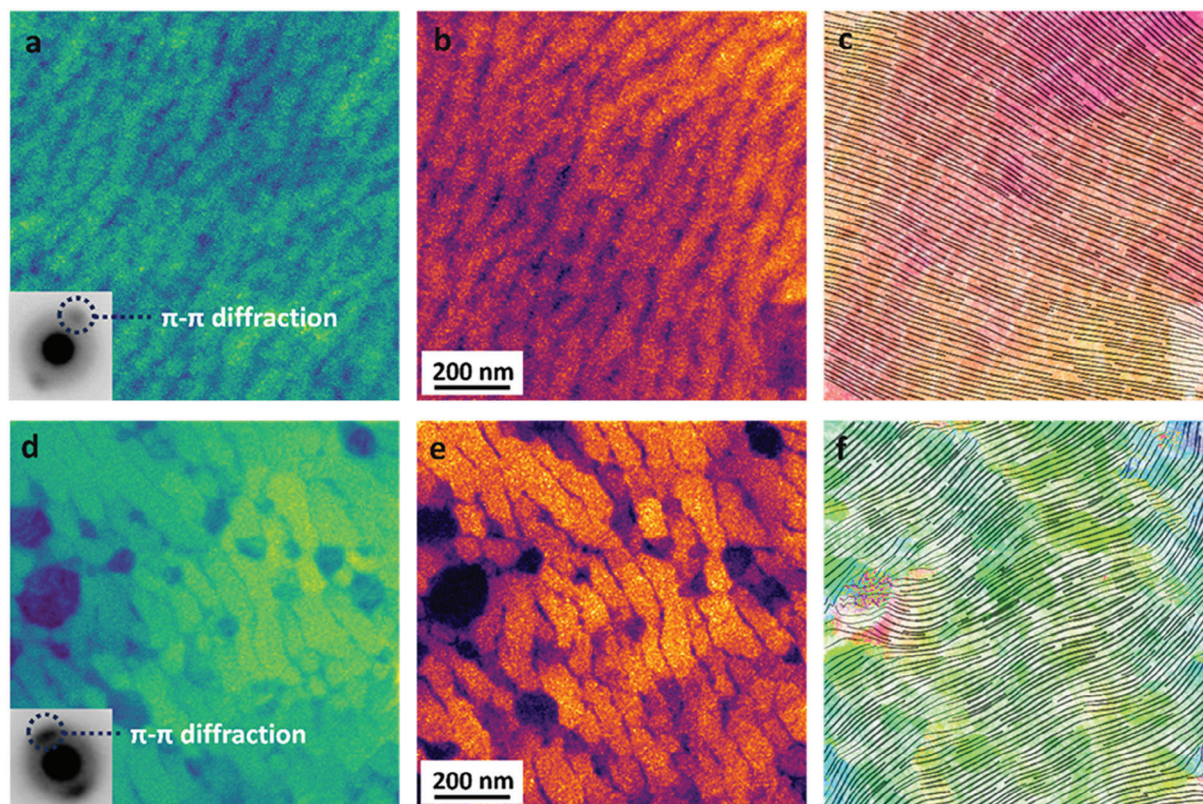


Figure 4. Crystalline order across individual grain boundaries investigated by 4D-STEM: a) Annular dark field (ADF) and corresponding summer diffraction pattern (inset) of P1; b) corresponding virtual dark field image from π - π stacking showing the regions of strong chain-chain ordering; c) fitted chain orientation map of P1; d) ADF image and corresponding summer diffraction pattern (inset) of a blend film. e) Corresponding virtual dark field image from π - π stacking showing the regions of strong chain-chain ordering; f) fitted chain orientation map of the blend films. In the orientation maps, only the dominant order is shown.

than in the blend films. This suggests that the highly crystalline ribbon domains of the P1 films do not allow incorporation of the longer chains as tie chains, but instead, the longer chains are accommodated fully in a relatively wide domain boundary region. In contrast, the blend films exhibit slightly lower crystalline order, as evident from the GIWAXS and DSC; this makes incorporation of tie chains energetically less prohibited, leading to an overall chain straightening effect in the domain boundaries and as a result a narrower domain boundary. In the ADF images we also detected regions where the grain boundary contrast disappeared, that is, where adjacent ribbons appeared to merge. These are highlighted in Figure 4e. It appeared that these were more prominent in blend films than in P1 films, in the latter these were essentially absent. Both observations are interpreted as a manifestation of tie chain incorporation and could be directly related to the conductivity behavior, that is, narrower grain boundaries are likely to result in faster ribbon-to-ribbon transport and higher conductivity. However, a more quantitative, statistical analysis of the interconnectivity of the ribbons, was challenging due to sample-to-sample variations in the fabrication protocol for the 4D-STEM samples. We were unable, for example, to produce as highly aligned films of P2 on the TEM grids (Figure S6, Supporting Information) though for the blend and P1 films, the results were reproducible (Figure S7, Supporting Information).

2.3. The Spectroscopic Characterization

We also undertook a careful spectroscopic characterization of the films. Polarized ultraviolet-visible (UV-vis) spectroscopy was used to quantify the degree of chain alignment through the dichroic ratio $R = A_{\parallel}/A_{\perp}$, where A_{\parallel} and A_{\perp} represent the peak absorbance at either the 0-0 or 0-1 vibrational peak. The dichroic ratio reached a value of 12.7 for undoped blend films at the neutral π - π^* absorption band of 553.1 nm (Figure 5a) and 8.9 for doped blends at the polaron-induced absorption band at 875.0 nm (Figure 5b). Both transitions are known to be polarized along the polymer chain axis and the dichroic ratio provides therefore a quantitative measure of overall chain alignment. Very similar dichroic ratios were also observed in P1 and P2 films, which demonstrates that high and comparable degree of chain alignment was achieved in all three polymer films, which is consistent with the GIWAXS data. To compare the degree of energetic disorder photothermal deflection spectroscopy (PDS) was carried out on the undoped films (Figure 5c), which provides a bulk-sensitive probe of the sub-bandgap tail of the excitonic joint density of states and allows extracting the Urbach energy E_u from an exponential fit in the sub-bandgap region.^[15] P1 exhibited a slightly lower E_u of 50.3 meV than P2 (51.6 meV) and P3 (51.1 meV). This could indicate higher crystalline order with fewer torsional defects in P1, which is consistent with the DSC. However,

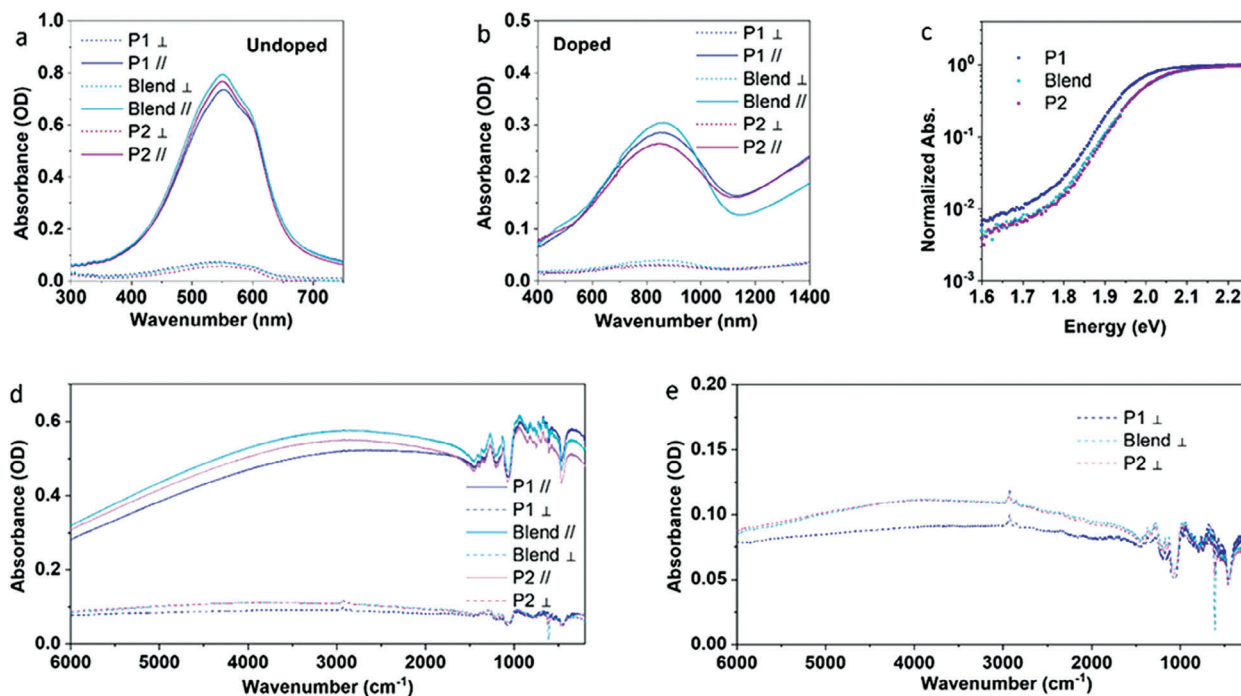


Figure 5. Searching for spectroscopic signatures of differences in microstructure: a) Polarized ultraviolet-visible spectroscopy of the undoped samples from which the dichroic ratio induced by the chain alignment can be determined. b) Polarized ultraviolet-visible spectroscopy of the doped samples. c) Photothermal deflection spectroscopy (PDS) of the polymers, d) polarized mid-IR spectra of the doped films for incident light polarized parallel and perpendicular to the chain alignment direction. e) Enlarged figure of the spectra in (d) for incident light polarized perpendicular to the chain alignment.

the differences in E_{μ} are close to the measurement accuracy of PDS. More convincing evidence for a slightly higher degree of crystalline order in P1 may be the observation of a slight lowering of the band gap E_g extracted from power law fits of the optical absorption.

Polarized Fourier-transform infrared (FTIR) spectroscopy was used on doped films to measure the polaron-induced absorption in the mid-IR which provides a sensitive probe of the degree of polaron delocalization. Two peaks are typically observed that are referred to as the B peak around $3500\text{--}2500\text{ cm}^{-1}$ and the A peak around 1000 cm^{-1} . A redshift of the B peak and a more intense A peak are signatures of a more pronounced polaron delocalization along the chains and in the interchain direction.^[16] The spectra taken with the polarizer along the blade coating direction (Figure 5d), which are sensitive mainly to the polarons sitting on the highly aligned chains in the crystalline domains, indicate that polarons in the crystalline domains of P1 are slightly more delocalized than those in P2 and blend films, while P2 and blends films exhibit similar polaron delocalization. This is also consistent with a lower degree of torsional defects and longer conjugation length in the crystalline domains of P1. When the polarizer is aligned perpendicular to the blade coating direction, the spectra preferentially probe polarons sitting in the less well-aligned grain boundary regions (Figure 5e). These are clearly more localized than those in the crystalline regions, which is consistent with the more disordered chain conformation expected in the grain boundaries. Overall, the spectroscopic characterization shows that although there are subtle differences in the crystalline order of the three samples, with P1 exhibiting longer conjugation lengths and more delocalized polarons, these cannot be respon-

sible for the observed conductivity behavior, as they would imply that P1 should exhibit the highest conductivity.

Based on the evidence from Figures 2–5, we conclude that tie chain incorporation provides indeed the only consistent explanation of the conductivity enhancement: P1 films are the most crystalline as evident from DSC, GIWAXS, and optical spectroscopy, but exhibit wide grain boundaries with an absence (or low concentration) of tie chains across them. The blend films are slightly less crystalline, but they have narrower grain boundaries with tie chains facilitating the transport across them (Figure 1a). We also propose a hypothesis as to why the P2 films do not exhibit as high conductivity as the optimized blends. This cannot be due to differences in structural order in the crystalline domains, as paracrystallinity values for blends and P2 films are very similar and also the polarons in the crystalline domains exhibit very similar degrees of localization. It must therefore also reflect differences in the grain boundary structure. We postulate that the high concentration of hairpin chain folds that is present in the P2 films could increase the degree of structural and energetic disorder in the grain boundaries and could limit the ability of the polymer chains to become incorporated as straight tie chains. In contrast, in the blend films, there are likely to be fewer chain folds and the longer chains are likely to find it easier to remain more chain extended and cross over into the next crystalline domains.

2.4. The Thermoelectric Properties

We investigated how such controlled tie chain incorporation affects the temperature-dependent thermoelectric transport

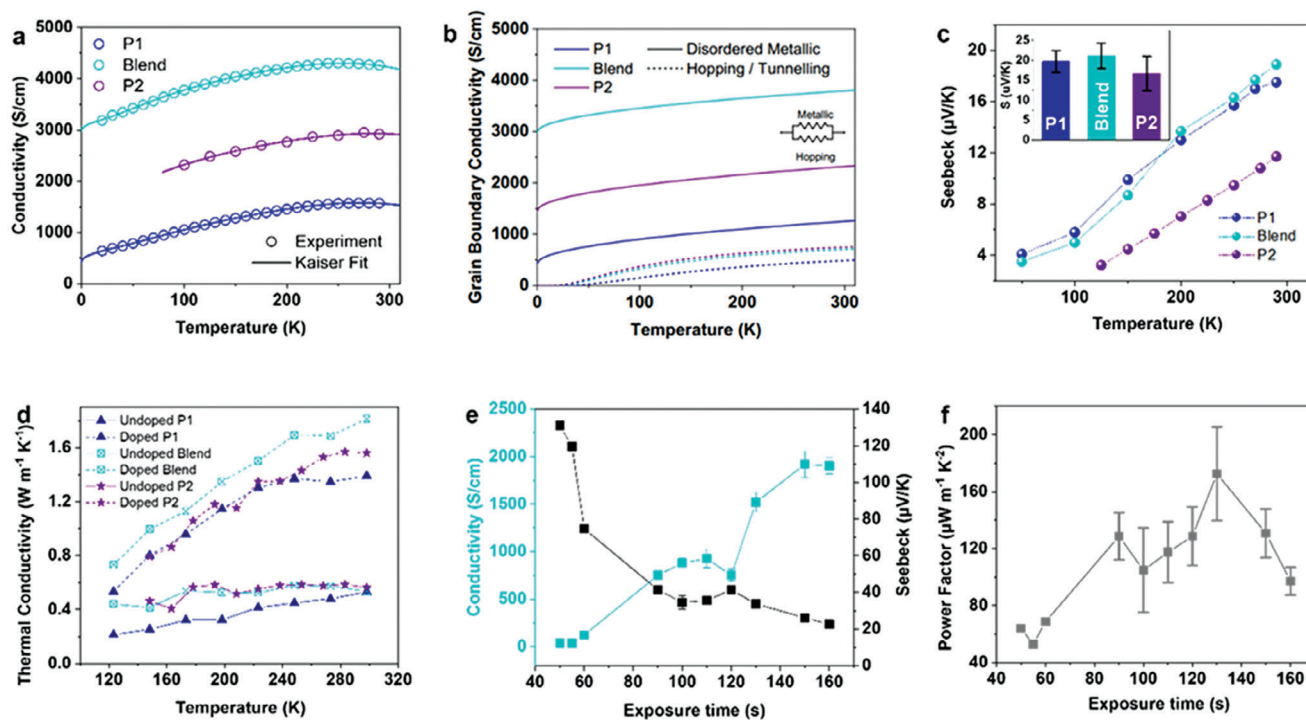


Figure 6. Effect of tie chain incorporation on thermoelectric properties: a) Temperature-dependent electrical conductivity of the doped polymers. Circles represent experimental data, lines represent fittings according to the Kaiser model (Section S6, Supporting Information). b) Grain boundary conductivities obtained by Kaiser model fits. The model includes two parallel conduction pathways: disordered metallic conduction (solid lines) and hopping/tunneling conduction (dashed lines). c, d) Temperature-dependent thermoelectric transport coefficients of P1, P2, and the blends measured at the maximum conductivity obtained with a FeCl_3 dopant concentration of 1 mM: c) Temperature-dependent Seebeck coefficient; the inset represents the distribution of Seebeck coefficient values measured on multiple samples at room temperature. d) Temperature-dependent thermal conductivity of the doped and undoped samples. e, f) Dependence of the room temperature thermoelectric properties of the blends on the exposure time to the doping solution for two different FeCl_3 concentrations: e) electrical conductivity and Seebeck coefficient, f) power factor.

coefficients in the plane of the film (Figure 6a–c). For accurate four-point probe conductivity and Seebeck measurements we used an on-chip microfabricated device architecture with integrated heaters and calibrated temperature sensors, for which the polymer film was patterned into a Hall bar.^[17] The electrode pattern is shown in Figure S8, Supporting Information, and the influence of alignment on thermoelectric properties is shown in Figure S9, Supporting Information. In all three polymers the conductivity shows a broadly similar temperature dependence typical for high conductivity PBTTT with a flattening or even decrease above 250 K (Figure 6a). This conductivity peak is typically understood as originating from heterogeneous charge transport, due to competition between phonon scattering within metallic grains, and thermally activated hopping in disordered grain boundaries.^[5b] Following from this indication of heterogeneous transport, we fit the data in Figure 6a using a well-known heterogeneous transport model by Kaiser and Graham (solid lines in Figure 6a, details in Section S6, Supporting Information).^[18] Briefly, the Kaiser model describes conduction as occurring by metallic conduction within crystallites, in series with two parallel grain boundary conduction pathways: hopping/tunneling and disordered metallic. The fits confirm our underpinning hypothesis that, for all samples and temperatures, grain boundary resistance is at least an order of magnitude greater than intragrain metallic transport and therefore that grain bound-

aries strongly limit conductivity. Figure 6b shows the conductivity of the two parallel grain boundary conduction pathways, hopping/tunneling (dashed lines) and disordered metallic (solid lines). The hopping conductivity contribution in the blend and P2 samples is higher than in P1. However, in all samples grain boundary conductivity, and thus the macroscopic sample conductivity, is dominated by the disordered metallic pathway. Metallic grain-boundary conduction necessarily requires carrier delocalization within grain boundaries, and thus a relatively straight, low-torsion tie chains spanning between crystallites. Our fits therefore indicate that conductivity in all samples is strongly tie-chain limited, and that an increased density of tie chains is directly responsible for strongly enhanced conductivity in the blend sample compared to P1 and P2. The Seebeck coefficient (Figure 6c) varies linearly with temperature, in good agreement with the Mott formula for metals and previous measurements on ion exchange doped PBTTT.

Thermal conductivity is the third relevant transport coefficient for thermoelectric materials.^[1a] In all samples the thermal conductivity is temperature activated (as shown in Figure 6d), which is typical for disordered materials. Interestingly, we find that the thermal conductivity of the undoped samples κ_1 , which is governed by the contribution from lattice vibrations, is much less strongly affected by the incorporation of tie chains than the electrical conductivity. This suggests that grain boundaries

constitute less of a bottleneck for phonon transport than they do for charge transport. In the blends and P2, κ_1 is only about 25% higher than in P1 at room temperature. The doped samples exhibit significantly higher thermal conductivity, which reflects the contribution κ_e from the heat carried by charge carriers. However, the increase is not as large as would have been expected from the Wiedemann-Franz relationship $\kappa_e/\sigma = LT$, particularly in the blends. If the Lorenz number L was equal to its free electron value $L = \pi^2/3 (k_b/e)^2 = 2.44 \cdot 10^{-8} \text{ V}^2 \text{ K}^{-2}$ we would have expected the thermal conductivity of the blend films to exceed values of $3 \text{ W m}^{-1} \text{ K}^{-1}$. Our observation that the thermal conductivity of the highly electrically conducting P2 samples is limited to $1.83 \text{ W m}^{-1} \text{ K}^{-1}$ therefore suggests that the free-electron Wiedemann-Franz relationship is violated in this system. An alternative explanation is the possibility that upon doping the lattice thermal conductivity is reduced, as was previously observed for PBTTT by the Campoy-Quiles's group based on comparing undoped and very lightly doped films.^[1a] However, we note that our lattice thermal conductivities in the undoped films are lower than what was reported in ref.^[19] and there is therefore limited scope for a further reduction upon doping.

To provide an assessment of the thermoelectric performance achievable in our PBTTT model system we carried out an optimization of the blends as a function of doping concentration. The result of Figure 6a–d is from films doped to maximum conductivity with 1 mM of FeCl_3 . However, we found it difficult to adjust the doping level with such a high dopant concentration; already after 3 s the films were highly doped and reached an electrical conductivity of 1805 S cm^{-1} (Figure S13, Supporting Information). Therefore, we used 0.33 mM of FeCl_3 instead to achieve a more controlled modulation of thermoelectric properties. As expected the electrical conductivity of blend films was found to increase with exposure time while the Seebeck coefficient decreases (Figure 6e). A maximum power factor of $173 \mu\text{W m}^{-1} \text{ K}^{-2}$ was reached at the exposure time of 130 s (Figure 6f), which is competitive to other values reported in the literature for PBTTT,^[19] though it is not as high as the value reported,^[3b] which to the best of our knowledge has not been verified independently yet. In previous work on aligned PBTTT, the thermal conductivity was not measured, but our measurements reported here allow us to estimate the figure-of-merit for thermoelectric performance, $ZT = S^2\sigma T/\kappa$ to be on the order of 0.04–0.05. This remains an order of magnitude below the best values reported for PEDOT-based conjugated polymers,^[20] which is mainly due to the relatively low value of S that is achievable in our ribbon-phase PBTTT model system. It is evident that competitive values of ZT could be achieved by applying our approach to materials systems that exhibit higher Seebeck coefficients on the order of $100 \mu\text{V K}^{-1}$; this will be a focus of our research in the future.

3. Conclusion

We have demonstrated a model system for the controlled incorporation of tie-chains into semicrystalline conjugated polymers using blends of different molecular weights that lead to a significant increase in electrical conductivity. Through careful assessment of the microstructural evolution upon tie chain incorporation, we have demonstrated that no major changes in phase morphology or structural order in the crystalline do-

main occur and that the observed enhancement in electrical conductivity can only be explained consistently by tie chains facilitating the transport across grain boundaries between the crystalline domains. Our approach allows overcoming some of the traditional trade-offs limiting thermoelectric performance: we can achieve a significant increase in conductivity without a reduction in Seebeck coefficient and the inevitable increase in thermal conductivity is not as large as expected from the free-electron Wiedemann-Franz law. Our approach should be generally applicable to a wide range of semicrystalline polymers and could provide a path to significant advances in the thermoelectric figure-of-merit of these promising thermoelectric materials systems.

4. Experimental Section

Materials: The first batch of PBTTT (poly(2,5-bis(3-alkylthiophene-2-yl)thieno(3,2-b)thiophene), denoted as P1, with $M_n = 28 \text{ kDa}$, $M_w = 40 \text{ kDa}$, $\text{PDI} = 1.45$ was synthesized as described previously.^[21] The second batch, denoted as P2, with $M_n = 35 \text{ kDa}$, $M_w = 58 \text{ kDa}$, $\text{PDI} = 1.68$, was purchased from 1-Material Inc. BMP-TFSI (1-butyl-1-methylpyrrolidinium bis(trifluoromethanesulfonyl)imide, >98.5%, <0.04% water) and FeCl_3 (anhydrous, >99.99% trace metals basis) were purchased from Sigma Aldrich. Anhydrous 1,2-dichlorobenzene (Romil Hi-Dry, <20 ppm water) was used for dissolving the polymers. Anhydrous acetonitrile (Romil Hi-Dry, <20 ppm water) was used to prepare FeCl_3 and BMP-TFSI solutions for the ion exchange doping. All materials were used as received.

Solution Preparation: PBTTT solutions (10 g L^{-1} , 1,2-dichlorobenzene (DCB)) were heated at $120 \text{ }^\circ\text{C}$ for 1 h before use. To prepare the blend solutions, defined volumes of P1 solution and P2 solution were mixed, the mixture was then heated at $120 \text{ }^\circ\text{C}$ for 10 min to be blended well. The BMP-TFSI solutions were prepared at 1 M concentration in acetonitrile. FeCl_3 solutions were prepared at 10 mM concentration in acetonitrile. FeCl_3 solutions were always prepared immediately before use. All solution preparation processes were performed in a glovebox under nitrogen atmosphere (<1 ppm of H_2O and O_2).

Alignment: Chain alignment was performed using a home-built blade coater located in a separate nitrogen glovebox (MBraun, <1 ppm O_2 , <1 ppm H_2O). A PTFE rod was used as the coating blade. $10 \mu\text{L}$ of the polymer solution was injected into the gap between the blade and the substrate. Then the temperature-controlled substrate ($80 \text{ }^\circ\text{C}$) moved at a fixed speed of $110 \mu\text{m}^{-1} \text{ s}$ underneath a PTFE coating blade. After blade coating, the deposited polymer on the substrate was annealed at $270 \text{ }^\circ\text{C}$ for 20 min, then cooling down to room temperature on hotplates naturally.

Ion Exchange Doping: Doping was performed on the spin coater by dropping $140 \mu\text{L}$ of 1 mM/100 mM FeCl_3 /BMP-TFSI in acetonitrile solution onto the pre-prepared films, keeping the solution on the substrates for 100 s, then spinning the excess off at 2000 rpm and washing with 1 mL of acetonitrile.

Conductivity Measurements: The thin film conductivity measurements at room temperature were performed using an Agilent 4155B semiconductor parameter analyzer in a nitrogen atmosphere (Belle Technology, <10 ppm O_2 , <20 ppm H_2O). Each device was isolated by scratching off the film outside the active device area before measurement. Film thickness was measured by surface profilometry (Bruker DekTak XT).

Temperature-Dependent Thermoelectric Measurements: PBTTT films were patterned into a Hall bar (420 by 105 micrometers) by photolithography and oxygen plasma etching process as detailed elsewhere.^[21] The temperature-dependent electrical conductivity and Seebeck coefficient evaluation were performed in a closed-cycle LakeShore Cryotronics CRX-4K probe station under high vacuum (10^{-7} to 10^{-6} mbar). A Keithley 2182A nanovoltmeter (for thermovoltage measurements) and a Keithley 2612B source-meter unit (for voltage sourcing and four probe conductivity measurements) were used for electrical measurements. The error analysis was performed following the report by Statz et al.^[22]

Temperature-Dependent Thermal Conductivity Measurements: To measure the thermal conductivity, the setup of a LINSEIS Thin Film Analyzer was used, which was an integrated system containing the following elements: a probe station with fixed probes with designed electrical connections, a cryogenic temperature controller with the operation temperature ranging from -100 to 300 °C, a vacuum pump connected to the chamber of the probe station, capable of making vacuum at a pressure between 10^{-7} and 10^{-4} mbar, depending on the environmental temperature, and a Stanford Research Systems Model SR830 DSP lock-in amplifier.

The measurement of thermal conductivity was based on the 3ω method using a suspended silicon nitride-based membrane with a thin metallic strip, which was in thermal contact with the organic film deposited onto the membrane. The metallic strip acts as both a heater and a temperature sensor. For the measurement of an AC current,

$$I(t) = I_0 \cos(\omega t) \quad (1)$$

with angular modulation frequency ω and amplitude passing through the strip, provides a heating source with power,

$$P(t) = I_0^2 R_h \cos^2(\omega t) \quad (2)$$

where R_h is the resistance of the strip under the experimental conditions. This causes a rise in the temperature in the form of,

$$\Delta T = \Delta T_0 \cos(2\omega t + \varphi) \quad (3)$$

and consequentially an oscillation in the resistance of the stripe:

$$R_h = R_{h0} (1 + \beta \Delta T) \quad (4)$$

This causes the resistance of the strip to oscillate with a frequency of 2ω and the measured voltage contains a component oscillating with 3ω . By measuring this component the temperature rise can be determined and this can be related to the thermal conductivity of the organic film on top of the membrane using Fourier's law. The implementation of this method on the Linseis thin film analyzer involved careful calibration of the thermal conductivity of the silicon nitride membranes on which the organic films were deposited and also included a correction for radiation, which involved measuring two membranes of different sizes. More details on the thermal conductivity measurements can be found in ref. [17].

GPC: Number-average (M_n) and weight-average (M_w) molar masses were determined by an Agilent Technologies 1200 series gel permeation chromatography (GPC) instrument running in chlorobenzene at 80 °C, using two PL mixed B columns in series, and calibrated against narrow polydispersity polystyrene standards.

FSC: FSC Experiments were performed on a Mettler-Toledo Flash DSC 1+ device, connected to an intracooler. For the measurements, multiSTAR UFS1 chip sensors were conditioned and corrected prior to use according to the specifications. Measurements were carried out under a nitrogen atmosphere. Prior to calorimetric measurements, samples were annealed at 295 °C for 15 min and then cooled down to 20 °C at 15 °C min^{-1} . The measurements consisted of recording heat flow rate during heating of the sample from -80 to 350 °C at 4000 °C s^{-1} .

AFM Measurements: Tapping Mode AFM measurements were performed on an Oxford Instruments Cypher ES Environmental AFM and with an RTESPA-150 probe (resonant frequency 150 kHz, spring constant 0.4 N m^{-1} , Bruker) to characterize the surface morphology of the samples at a scan rate of 0.5 Hz and 512 samples per line. The data were analyzed with Gwyddion 2.63 (open-source software), including the analysis of PBTBT ribbons by fast Fourier transform (FFT). The measurements to determine the melting points of pristine PBTBT ribbons were performed in an inert atmosphere protected by a continuous flow of dry N_2 , with an RTESPA-150 probe at a scan rate of 0.5 Hz and 512 samples per line. The temperature of the samples was controlled by a programmable sample stage (provided by Cypher ES Environmental AFM) and measured simultaneously by an external type-K thermocouple attached onto the sample. The melting point

of the samples was determined by the observation of the dissociation of the ribbon phase.

XPS Measurements: XPS spectra were collected on a Thermo Scientific Escalab 250xi. The pass energy of 20 eV, step size of 0.1 eV, spot size of 400 μm , and 30 scan averaging were used. Data was processed using CasaXPS software, and a Shirley background was used in all fits. Sulfur 2p spectra were characterized by a doublet ($2p_{3/2}$ and $2p_{1/2}$) with 2:1 area ratio and spin-orbit coupling $\Delta = 1.18$ eV.^[23] Error bars were estimated by a Monte Carlo process in CasaXPS.

GIWAXS Characterization: GIWAXS measurements were performed at Brookhaven National Lab at the 12-ID Soft Matter Interfaces (SMI) beamline of the National Synchrotron Light Source II (NSLS-II) with a beam energy of 16.1 keV. The 2D scattering patterns were collected at an X-ray incidence angle of 0.10° with a Pilatus 900 K-W detector with a pixel size of 172 μm placed at 279 mm from the sample. The sample and detector were enclosed in a vacuum chamber to suppress air scatter. To cover the range of scattering angles desired, the vertically oriented elongated detector was moved horizontally on a fixed arc and images were later visualized in Xi-CAM software and stitched and radially integrated using custom code.

Electron Microscopy: The PBTBT thin films were probed using scanning electron diffraction (SED), a 4D-STEM technique with a low (<1 mrad) convergence angle. SED data were acquired on a TS Spectra 300 operated at 300 kV with a convergence angle of ≈ 0.5 mrad and a diffraction-limited beam diameter of ≈ 6 nm. The current was ≈ 20 pA, with a frame time of 1 ms, leading to an electron fluence of ≈ 140 $\text{e}^- \text{\AA}^{-2}$. The diffraction patterns for SED were acquired using a single-chip Medipix3 direct electron detector (256 by 256 pixels) and a camera length of 145 mm, leading to a Δs of 0.0094 \AA^{-1} and to a maximum scattering vector of 1.1 \AA^{-1} . Additional data were collected under the same conditions at 200 kV.

Polarized Photothermal Deflection Spectroscopy: PDS was performed by a tunable light source consisting of a 250 -W quartz tungsten halogen lamp coupled with a 250 -mm focal length grating monochromator. The monochromatic excitation beam was modulated at 13 Hz. The sub-gap absorption data $A(E)$ were fitted to an exponential trail to extract the Urbach energy E_U .

Polarized UV-Vis Spectroscopy: UV-vis-NIR spectra were collected on a Shimadzu UV-3600i dual beam spectrometer, with a slit width of 3 nm and a data interval of 1 nm. The background spectra from the blank glass were collected separately.

Supporting Information

Supporting Information is available from the Wiley Online Library or from the author.

Acknowledgements

Financial support from the European Research Council for an advanced grant (no. 101020872) and the Engineering and Physical Sciences Research Council (EP/W017091/1) is gratefully acknowledged. W.Z. acknowledges the Winton Scholarship through her Ph.D. studies. H.S. acknowledges the support from a Royal Society Research Professorship (RP/R1/201 082). J.E.M.L. acknowledges financial support from EC H2020 (ESTEEM3, 823717), and P.A.M. thanks EPSRC for funding (EP/R008779/1, EP/V007785/1). H.-I.U. thanks the Engineering and Physical Sciences Research Council and the Japanese Society for the Promotion of Science (JSPS) for support through a core-to-core grant (EP/S030662/1). The authors thank Carmen Fernandez Posada for assistance with XPS measurements and the Henry Royce Institute for access to the XPS and thermal conductivity measurement equipment (Cambridge Royce facilities grant EP/P024947/1 and Sir Henry Royce Institute – recurrent grant EP/R00661X/1). The authors thank Suhao Wang, Suraj Manikandan, and Jens Wenzel Andreasen for assistance with GIWAXS data analysis. The authors thank Craig Yu and Robert Cornell for assistance with DSC measurements. This research used the Soft Matter Interfaces (SMI) beamline (Beamline 12-ID) of the National Synchrotron

Light Source II, a U.S. Department of Energy (DOE) Office of Science User Facility operated for the DOE Office of Science by Brookhaven National Laboratory under contract no. DE-SC0012704.

Conflict of Interest

The authors declare no conflict of interest.

Data Availability Statement

The data that support the findings of this study are available from the corresponding author upon reasonable request.

Keywords

ion exchange doping, organic thermoelectrics, polymer alignment, tie chains

Received: October 9, 2023

Revised: February 19, 2024

Published online:

- [1] a) O. Zapata-Arteaga, S. Marina, J. Martin, J. S. Reparaz, M. Campoy-Quiles, *ACS Energy Lett.* **2020**, *5*, 2972; b) S. Wang, G. Zuo, J. Kim, H. Sirringhaus, *Prog. Polym. Sci.* **2022**, *129*, 101548.
- [2] M. G. Kanatzidis, *Nat. Mater.* **2022**, *21*, 503.
- [3] a) Y. Huang, D. H. Lukito Tjhe, X. Huang, I. McCulloch, H. Sirringhaus, *Appl. Phys. Lett.* **2021**, *119*, 111903; b) V. Vijayakumar, V. Untilova, M. Bahri, L. Herrmann, L. Biniek, N. Leclerc, M. Brinkmann, *Adv. Energy Mater.* **2019**, *9*, 1900266; c) G. Giri, J. Reinspach, D. A. Fischer, L. J. Richter, J. Xu, S. Benight, A. Ayzner, M. He, L. Fang, G. Xue, M. F. Toney, Z. Bao, *Chem. Mater.* **2015**, *27*, 2350.
- [4] a) M. Xiao, S. B. Lee, L. M. A. Perdigão, A. Luci, D. A. Warr, S. P. Senanayak, M. Nikolka, M. Statz, Y. Wu, A. Sadhanala, S. Schott, R. Carey, Q. Wang, M. Lee, C. Kim, A. Onwubiko, C. Jellett, H. Liao, W. Yue, K. Cho, G. Costantini, I. McCulloch, H. Sirringhaus, *Adv. Mater.* **2020**, *32*, 2000063; b) L. Shaw, Y. Diao, J. A. Reinspach, J. W. F. To, M. F. Toney, R. T. Weitz, Z. Bao, *ACS Appl. Mater. Interfaces* **2016**, *8*, 9285; c) L. Biniek, T. Heiser, R. Bechara, M. Brinkmann, *Macromolecules* **2013**, *46*, 4014.
- [5] a) S. Fratini, M. Nikolka, A. Salleo, G. Schweicher, H. Sirringhaus, *Nat. Mater.* **2020**, *19*, 491; b) A. B. Kaiser, *Adv. Mater.* **2001**, *13*, 12.
- [6] a) R. Noriega, K. Vandewal, F. P. V. Koch, N. Stingelin, P. Smith, M. F. Toney, A. Salleo, *Nat. Mater.* **2013**, *12*, 1038; b) K. Gu, J. Onorato, C. K. Luscombe, A. W. Bosse, Y. Loo, *ACS Macro Lett.* **2018**, *7*, 1333.
- [7] M. J. Lee, N. Zhao, M. Heeney, I. McCulloch, H. Sirringhaus, *Adv. Funct. Mater.* **2011**, *21*, 932.
- [8] T. Hallam, N. Zhao, I. Nandhakumar, M. Kemerink, M. Heeney, I. McCulloch, H. Sirringhaus, *Phys. Rev. Lett.* **2009**, *103*, 256803.
- [9] a) I. E. Jacobs, Y. Huang, X. Ren, D. Simatos, C. Chen, D. Tjhe, M. Statz, L. Lai, P. A. Finn, W. G. Neal, G. D'Avino, V. Lemaury, S. Fratini, D. Beljonne, J. Strzalka, C. B. Nielsen, S. Barlow, S. R. Marder, I. McCulloch, H. Sirringhaus, *Adv. Mater.* **2021**, *34*, 2102988; b) Y. Yamashita, J. Tsurumi, M. Ohno, R. Fujimoto, S. Kumagai, T. Kurosawa, T. Okamoto, J. Takeya, S. Watanabe, *Nature* **2019**, *572*, 634.
- [10] J. Martín, D. Cangialosi, *J. Phys. Chem. Lett.* **2018**, *9*, 990.
- [11] C. Greco, A. Melnyk, K. Kremer, D. Andrienko, K. Ch Daoulas, *Macromolecules* **2019**, *52*, 968.
- [12] I. E. Jacobs, V. Lemaury, Y. Lin, Y. Huang, C. Chen, T. F. Harrelson, W. Wood, L. J. Spalek, T. Mustafa, C. A. O'Keefe, X. Ren, D. Simatos, D. Tjhe, M. Statz, J. W. Strzalka, J. Lee, I. McCulloch, S. Fratini, D. Beljonne, H. Sirringhaus, *J. Am. Chem. Soc.* **2022**, *144*, 3005.
- [13] E. Cho, D. Kim, R. Gysel, N. C. Miller, D. W. Breiby, M. D. McGehee, M. F. Toney, R. Joseph Kline, J. Bredas, *J. Am. Chem. Soc.* **2012**, *134*, 6177.
- [14] J. Rivnay, J. E. Northrup, R. J. Kline, M. F. Toney, A. Salleo, *Phys. Rev. B* **2011**, *83*, 121306.
- [15] D. Venkateshvaran, A. Sadhanala, V. Lemaury, M. Zelazny, M. Kepa, M. Hurhangee, A. J. Kronemeijer, V. Pecunia, I. Nasrallah, I. Romanov, K. Broch, I. McCulloch, D. Emin, Y. Olivier, J. Cornil, D. Beljonne, H. Sirringhaus, *Nature* **2014**, *515*, 384.
- [16] M. B. Qarai, R. Ghosh, F. C. Spano, *J. Phys. Chem. C* **2021**, *125*, 24487.
- [17] E. Selezneva, X. Jiao, C. R. McNeill, H. Sirringhaus, *APL Mater.* **2019**, *7*, 081118.
- [18] A. B. Kaiser, S. C. Graham, *Synth. Met.* **1990**, *36*, 367.
- [19] S. N. Patel, K. A. Peterson, E. M. Thomas, K. A. O'Hara, E. Lim, M. L. Chabinyc, *Sci. Adv.* **2017**, *3*, 1700434.
- [20] Y. Yang, H. Deng, Q. Fu, *Mater. Chem. Front.* **2020**, *4*, 3130.
- [21] J. Chang, M. Caironi, T. Sakanoue, H. Sirringhaus, *Adv. Funct. Mater.* **2010**, *20*, 2825.
- [22] M. Statz, X. Jiao, S. Schott, C. R. McNeill, D. Emin, H. Sirringhaus, R. Di Pietro, *Commun. Phys.* **2018**, *1*, 16.
- [23] D. A. Shirley, *Phys. Rev. B* **1972**, *5*, 12.